Synthetic Aperture Radar without Fourier Transforms

Jordan Mann * Robert Hummel
Courant Institute of Mathematical Sciences
New York University

December, 1992

Abstract

By viewing the radar chirp as a real-valued signal, the synthetic aperture radar (SAR) image reconstruction problem may be solved using a backprojection algorithm in the spatial domain incrementally as radar return signals are obtained. The resulting SAR algorithm, also studied by Desai and Jenkins [4], permits parallelization of the image reconstruction, and obviates a costly Fourier-domain resampling step. We further show that by using a chirp signal of a specially-designed form, the reconstruction becomes extremely simple, eliminating the need for Fourier processing of the return signals, by incorporating a derivative of a Hilbert transform into the emitted signal. We show some simulation results using this new method.

1 Introduction

Synthetic aperture radar (SAR) is a method of obtaining high-resolution imagery of a scene by means of radar signals. SAR images of the surface of Mars or of a distant country, for example, may be produced without actually traveling to Mars or flying over the country. Instead, radar signals are sent from a set of distant positions, and an image is reconstructed from the returns obtained at these multiple positions. Like computed-tomography, SAR involves reconstruction of a scene from its Radon transforms; that is, the reflected signal resulting from a radar "chirp" provides information about line integrals of the scene rather than information about the scene at individual points. However, unlike computed tomography, the reconstruction method used for SAR typically involves computations in the Fourier domain. Indeed, the most expensive step in conventional SAR image reconstruction involves interpolation of spectral values on a rectangular coordinate grid, given spectral values on a polar coordinate grid. This step typically requires the processing power of a supercomputer in order to obtain high-resolution imagery with a tolerable delay in time.

We describe below a reconstruction method for SAR that operates in the spatial domain and does not use Fourier transforms. Due to the simplicity of the computations, the method should

*This work forms a portion of the PhD dissertation of Jordan Mann. Research leading to this work was supported in part by AFAL Contract No. F33615-89-C-1089 Work Unit 87-02-PMRE. Thanks to Ed Zelnio who suggested this line of research.

significantly reduce the required computation time. The reconstructed image is built up incrementally, so that as each return chirp is received, every pixel in the output image is updated (by an accumulating sum), and intermediate results are available even before all the radar data has been collected. Further, the return signals need practically no processing. The data used to update the image is the data that is returned from the radar chirp. The results come about by defining the chirp signal in a precise manner; one possible chirp is built up using wavelets. We will show simulation results.

2 Background

SAR image reconstruction is possible because the information contained in a sampling of the Radon transform of an image is sufficient to produce an acceptable version of the original image. The fundamental problem of reconstructing a function of n variables from its integrals along hyperplanes was first studied by Radon [11], and hence the name the Radon transform. The transform, in its two-dimensional version in particular, has found applications in such diverse fields as radio astronomy, molecular biology, and computer-assisted tomography [7].

The use of Radon transform inversion methods has been successfully applied to SAR [1,8]. However, the reconstruction method that is typically used involves building a version of the Fourier transform of the image, and then performing an inverse Fourier transform. This approach is especially convenient because a simply-produced chirp can provide Fourier data in the spectral domain almost directly. The key to this is the projection slice theorem [8], which relates the Fourier transform of the image to the Fourier transform of the Radon transform of the image, which is embedded in the return signal. However, the approach is handicapped in two ways: first, the Fourier domain must be resampled in order to convert values from a polar grid representation to a rectangular grid, and second, the entire sampling process must be completed before an inverse Fourier transform is invoked in order to view the image.

Recently, Munson *et al.* [8] have suggested that the method of backprojection, which is typically used for computer tomography (CAT) imagery reconstruction, could also be applied to SAR image formation. The idea would be to build up the reconstructed image in the spatial domain, by means of the backprojection algorithm, rather than building up values in the spectral domain of the image.

This suggestion has been successfully tested by Desai and Jenkins [4]. They show that using the standard chirp signal, reconstructing the Fourier data of the Radon transform of the image using the return signal, and processing that return signal with a derivative of a Hilbert transform filter, they can make use of the backprojection method to build up the reconstructed image incrementally. The advantage of the method is that the resampling in Fourier space is unnecessary, and that intermediate versions of the reconstructed image are available as the return radar chirps are processed.

Motivated by Munson, our work makes use of the backprojection algorithm, exactly like Desai and Jenkins, and shares the advantages as described by them. Accordingly, much of our description here provides an independent presentation of the work of Desai and Jenkins. We add, however, an additional option, by going one step further in reducing the amount of processing required of the return signal. We propose to use a nonstandard chirp, which has built into it much of the processing that ordinarily must be done to the return radar signal. In this way, the return signal provides directly the values that are used to increment the accumulating spatial domain image. The normal

processing of the Radon transform data, which consists of applying the Hilbert transform followed by a differentiation, is no longer required. This step is usually not considered onerous because the Fourier data can be extracted from the return signal, but we obviate the need to perform this extraction as well. Notably, the new chirp signal is neither the amplitude nor frequency modulation of a carrier signal, but is a specifically designed function with specified and bandlimited spectral support.

3 Mathematical considerations

3.1 Classical approach

For reasons of convenience, it is custormary to regard the transmitted signal as a complex-valued function, although in reality only the real part of the function forms the intensity of the transmitted electromagnetic field. Here, we present an equivalent development in terms of real-valued functions.

In order to formulate the reconstruction methods, let us recall that $P_\theta f(t)$, the Radon transform of the function at angle θ, is defined by

$$P_\theta f(t) = \int_{-\infty}^{\infty} f(t\cos\theta - \tau\sin\theta, t\sin\theta + \tau\cos\theta)\, d\tau.$$

For any particular t, $P_\theta f(t)$ is the integral of the function along a line in the coordinate plane.

The Radon Slice theorem states that

$$\widehat{P_\theta f}(\rho) = \sqrt{2\pi}\hat{f}(\rho\cos\theta, \rho\sin\theta), \tag{1}$$

where the "hat" indicates the normalized Fourier transform. Thus that the 2-D Fourier transform of the image can be sampled by obtaining the Fourier transform of the Radon transform for different values of θ.

We note that if a point reflector at coordinates (x, y) is at a distance l from the radar, then the time it takes the signal to travel to the reflector and back is $2l/c$, where c is the speed of light. Thus, if the transmitted signal at time t is given by $s(t)$, then the signal returning to the radar antenna from the point reflector at (x, y) at time t is given by

$$g(x, y)s(t - 2l/c),$$

where $g(x, y)$ is the reflectivity of the reflector. If the imaging region is small with respect to the distance of the imaging region from the antenna, then the set of image points lying a distance l from the antenna lie approximately on a straight line, so the integral of the reflectivity function over those points is approximately equal to $P_\theta g(l)$, where θ is the angle between a line of reference and the line connecting the antenna and the center of the imaging region. Thus the accumulated signal at time t returning from distributed reflectors at a distance l is given by

$$P_\theta g(l)s(t - 2l/c).$$

The total returning signal must be integrated over points at all distances; thus the total returning signal at time t is given by

$$r(t) = \int P_\theta g(l)\, s(t - 2l/c)\, dl.$$

In the classical SAR system, the radar transmits a linear FM chirp pulse of the form

$$s(t) = \cos(\omega_0 t + \alpha t^2),$$

where ω_0 is the carrier frequency and 2α is the frequency modulation rate. As explained in [8], the return signal is processed in order to obtain the Fourier transform of $P_\theta g$. First, the return is mixed (multiplied) with the chirp $s(t)$ to obtain

$$\frac{1}{2}\int P_\theta g(l)[\cos(\omega_0(2t - \frac{2l}{c}) + \alpha(t^2 + (t - \frac{2l}{c})^2)) + \cos(\frac{4\alpha l^2}{c^2} - \frac{2l}{c}(\omega_0 + 2\alpha t))]\, dl.$$

The first cosine term, as a function of t, is centered on the carrier frequency ω_0, whereas the second cosine term is in the low-frequency domain, so that applying a low-pass filter to the mixed signal leaves

$$\frac{1}{2}\int P_\theta g(l)\cos(\frac{4\alpha l^2}{c^2} - \frac{2l}{c}(\omega_0 + 2\alpha t))\, dl. \tag{2}$$

Similarly, mixing the return signal with

$$\sin(\omega_0 t + \alpha t^2)$$

and applying a low-pass filter gives

$$\frac{1}{2}\int P_\theta g(l)\sin(\frac{4\alpha l^2}{c^2} - \frac{2l}{c}(\omega_0 + 2\alpha t))\, dl. \tag{3}$$

The integration over l is limited to a range of distances covering the region of interest. Thus l can be replaced by $l_0 + l'$, where l' becomes the new variable of integration and is relatively small. By discarding a quadratic term in l' which is very small for the entire region of interest, we can show that (2) and (3) constitute the real and imaginary parts respectively of $z(t)\widehat{P_\theta g}(\frac{2}{c}(\frac{l_0}{c} + \omega_0 + 2\alpha t))$, where $z(t)$ is a known complex function of t and $|z| = 1$. Multiplication by $\bar{z}(t)$ yields $\widehat{P_\theta g}$. These Fourier data are sampled at discrete points, and by the Radon slice Theorem, the values at those points are proportional to the values of the Fourier transform of the image at points on a "polar grid" in the Fourier domain (see Figure 1).

At this point, one has spectral data, i.e., samples of $\hat{g}$, at points on a polar grid. An inverse FFT is desired. Two problems arise: Large portions of the spectral domain are missing, and FFT's and inverse FFT's typically operate on rectangular, not polar, grids. The first problem is inherent in the system, and is generally ignored, since it does not necessarily result in significant image deterioration. The classical SAR method uses a time-consuming polar-to-rectangular interpolation in the Fourier domain to solve the second problem.

3.2 The modified Convolution-Backprojection method

Desai [3,4] has shown that the need for interpolation in the Fourier domain can be avoided by adapting the well-known convolution-backprojection algorithm (CBP) of computed tomography for use in SAR. In this algorithm, it is assumed that Fourier data are known on a polar grid, and reconstruction is performed based on the following. The Fourier transform inversion formula can be written in polar coordinates as

$$g(x,y) = \frac{1}{2\pi}\int_0^\pi \int_{-\infty}^{\infty} \hat{g}(\rho\cos\theta, \rho\sin\theta)\, e^{i(x\cos\theta + y\sin\theta)}|\rho|\, d\rho\, d\theta.$$

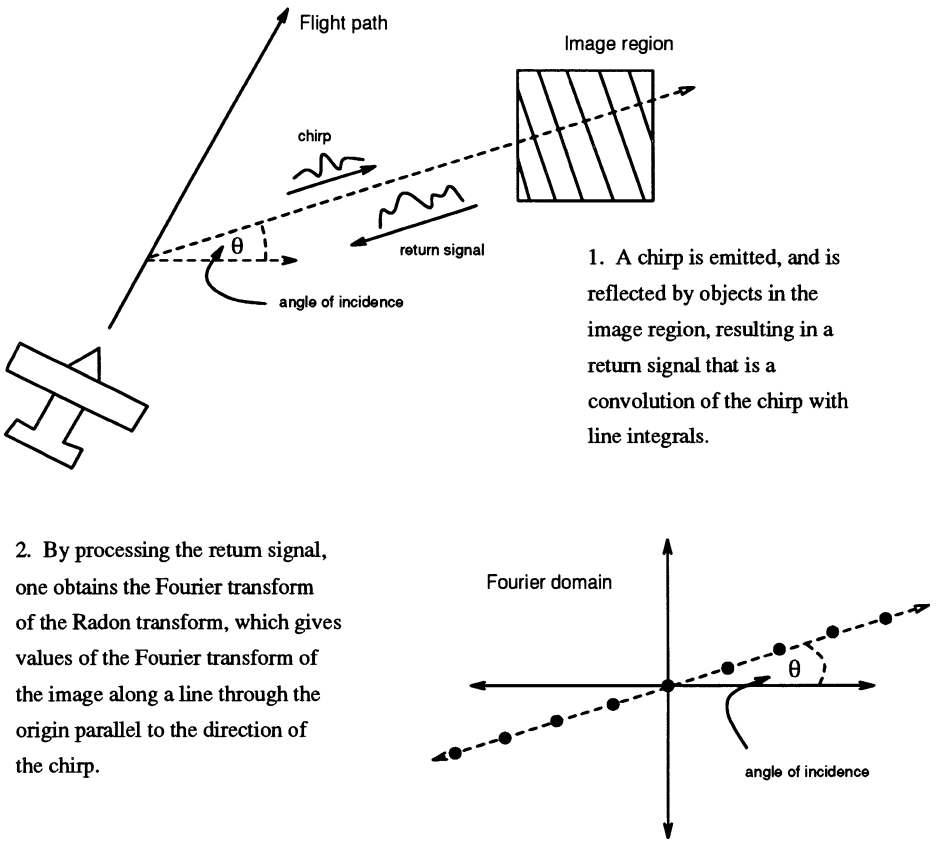

Figure 1: The classical approach to SAR image formation.
A radar chirp is emitted at discrete points along a flight path, and the return signals are processed to yield Fourier data of the image along a radial axis. This data is eventually resampled on a rectangular grid, and the image is formed from an inverse Fourier transform.

By the Radon Slice Theorem, this equals

$$\frac{1}{(2\pi)^{3/2}} \int_0^{\pi} \int_{-\infty}^{\infty} \widehat{P_\theta g}(\rho)\, e^{i(x\cos\theta + y\sin\theta)} |\rho|\, d\rho\, d\theta.$$

Now, the $\widehat{P_\theta g}$ values are made available by the mixing and filtering process, as described in the previous subsection. Using the $\widehat{P_\theta g}$ values, we may compute

$$\tilde{P}_\theta g(u) = \int_{-\infty}^{\infty} \widehat{P_\theta g}(\rho)\, e^{i\rho u} |\rho|\, d\rho.$$

This is easily computed numerically by means of multiplication and inverse FFT. Thus we can see that

$$g(x,y) = \frac{1}{(2\pi)^{3/2}} \int_0^{\pi} \tilde{P}_\theta g(x\cos\theta + y\sin\theta)\, d\theta,$$

which means that $g(x,y)$ can be reconstructed from the $\tilde{P}_\theta$ values, given these values for all θ. In practice, pixel (x,y) simply sums $\tilde{P}_\theta g(x\cos\theta + y\sin\theta)$ for all available values of θ. This method has several advantages. It avoids interpolation in the Fourier domain. Also, it allows a two-fold parallelization. First, the function $\tilde{P}_\theta g$ for a particular value of θ is computed entirely from the values of $\widehat{P_\theta g}$ for the same value of θ, so the Fourier data derived from each transmitted signal can be processed and applied incrementally to the image domain as soon as the reflected signal is received, mixed, and filtered. Secondly, for any angle θ, the values of $\tilde{P}_\theta g(x\cos\theta + y\sin\theta)$ for different points (x,y) can be computed independently of each other, allowing parallelization over the image.

3.3 SAR reconstruction using spatial filtering — the Wavelet-Based Chirp method

Since the emission and reflection of the signal implement a convolution of the signal with the Radon transform data, it is desirable to use a chirp that implements as much of the reconstruction process as possible. A signal can be produced that preprocesses the return signal and obviates the need to compute $\tilde{P}_\theta g$. We form such a chirp by making use of wavelets, and verify the resulting method analytically and empirically.

With the spatial filtering method, the convolution of $P_\theta g$ with the chirp signal (which we may call the convolving function) is the first step in the reconstruction technique. In this way, the convolution of $P_\theta g$ with the transmitted signal is no longer a minor nuisance, but the first step in the solution. If the spectral response of the chirp signal equals $|\rho|$, where ρ is the 1-D spectral domain variable, then no interpolation or inverse Fourier transform is required; if $r_\theta(t)$ is the signal returned at angle θ, then $g(x,y)$ is obtained simply by accumulating $r_\theta(x\cos\theta + y\sin\theta)$ at location (x,y), thereby building up $g(x,y)$ as θ varies. In this way, we retain all the advantages of the modified CBP method, and avoid the need to extract and process Fourier data from the return signal. As a bonus, the approximation based on the omission of a quadratic term in the Fourier data extraction is eliminated.

We will define a *pseudo-symmetric wavelet* as a function ψ in $L^2(\mathbf{R}^2)$ whose Fourier transform $\hat{\psi}$ is such that the value K_ψ defined by

$$K_\psi = (2\pi)^2 \int_0^{\infty} \frac{\hat{\psi}(\rho\cos\theta, \rho\sin\theta)}{\rho}\, d\rho \tag{4}$$

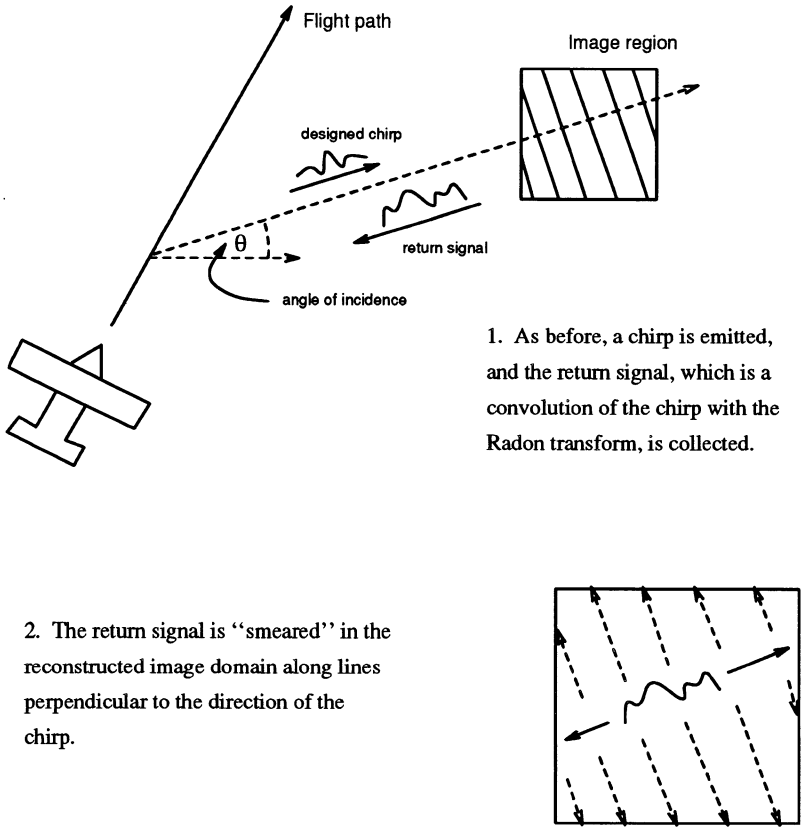

Figure 2: SAR reconstruction using spatial filtering.
A specially-designed chirp is emitted, and the return signal is sampled. If the chirp is of the appropriate form, no further processing is required. The image is reconstructed by accumulating data obtained from the return signal, where the incremental amount is constant along lines perpendicular to the direction of the chirp.

is finite and independent of the θ variable[1].

Given a function f in $L^2(\mathbf{R}^2)$ and a wavelet ψ, we define $W_s f(a,b)$, the wavelet transform of f at location (a,b) and scale s, by

$$W_s f(a,b) = (f * \tilde{\psi}_s)(a,b),$$

where

$$\psi_s(x,y) = s\psi(sx,sy)$$

and

$$\tilde{\psi}_s(x,y) = \overline{\psi_s(-x,-y)}.$$

Let us once again assume that $g(x,y)$ is the function to be reconstructed. We will derive a chirp function and a simple reconstruction formula using the chirp. By the wavelet transform inversion formula,

$$g(x,y) = \frac{1}{K_\psi} \int_0^\infty s\,(\psi_s * W_s g)(x,y)\,ds, \tag{5}$$

where K_ψ is given in (4). Writing the convolution on the right side as the inverse Fourier Transform of its own Fourier transform, and using the rules for Fourier transform of a convolution, we find that the right side of (5) is equal to

$$\frac{2\pi}{K_\psi} \int_0^\infty s \int_{-\infty}^\infty \int_{-\infty}^\infty \widehat{\psi_s}(\zeta,\xi)\,\widehat{\tilde{\psi}_s}(\zeta,\xi)\,\hat{g}(\zeta,\xi)\,e^{i(x\zeta+y\xi)}\,d\zeta\,d\xi\,ds$$

$$= \frac{2\pi}{K_\psi} \int_0^\infty s \int_{-\infty}^\infty \int_{-\infty}^\infty |\widehat{\psi_s}(\zeta,\xi)|^2\,\hat{g}(\zeta,\xi)\,e^{i(x\zeta+y\xi)}\,d\zeta\,d\xi\,ds$$

$$= \frac{2\pi}{K_\psi} \int_0^\infty s \int_0^\pi \int_{-\infty}^\infty |\widehat{\psi_s}(\rho\cos\theta,\rho\sin\theta)|^2\,\hat{g}(\rho\cos\theta,\rho\sin\theta)\,|\rho|\,e^{i\rho(x\cos\theta+y\sin\theta)}\,d\rho\,d\theta\,ds. \tag{6}$$

Let

$$C_{s,\theta}(v) = \frac{1}{\sqrt{2\pi}} \int_{-\infty}^\infty |\widehat{\psi_s}(\rho\cos\theta,\rho\sin\theta)|^2\,|\rho| e^{i\rho v}\,d\rho,$$

and let

$$C_\theta(v) = \frac{1}{\sqrt{2\pi}} \int_{-\infty}^\infty |\hat{\psi}(\rho\cos\theta,\rho\sin\theta)|^2\,|\rho|\,e^{i\rho v}\,d\rho.$$

It can be shown by changes of variable that $C_{s,\theta}(v) = C_\theta(sv)$. As we will need $C_{s,\theta}$ and C_θ to be real, it is necessary and sufficient to require that

$$|\hat{\psi}(-\xi,-\zeta)| = |\hat{\psi}(\xi,\zeta)| \tag{7}$$

almost everywhere. Condition (7) holds, for example, if ψ is real or radially symmetric. Clearly,

$$\widehat{C_{s,\theta}}(\rho) = |\widehat{\psi_s}(\rho\cos\theta,\rho\sin\theta)|^2\,|\rho|.$$

[1]Following Mallat [6], a 2-D wavelet satisfies this condition, whereas Daubechies points out a generalization in which K_ψ varies with θ. A radially symmetric wavelet will of course have a K_ψ independent of θ, although radial symmetry is not necessary.

Thus equation (5) is equivalent to

$$g(x,y) = \frac{\sqrt{2\pi}}{K_\psi} \int_0^\infty s \int_0^\pi (P_\theta g * C_{s,\theta})(x\cos\theta + y\sin\theta)\, d\theta\, ds. \tag{8}$$

This formula may be simplified further. Let us suppose that g is wavelet band-limited, by which we mean that there exists $T > 0$ such that for all $s > T, W_s g(a,b) = 0$ for all (a,b). This is conceptually similar to the usual notion of band-limitedness, which is defined in terms of the Fourier transform. Then the integration with respect to s goes only up to T, not up to infinity, and it is possible to change the order of integration and integrate with respect to s first before doing the convolution. Integrating with respect to s, using $C_{s,\theta}(u) = C_\theta(su)$, where u is the variable of integration for the convolution, and making the change of variable $w = su$, we find that

$$g(x,y) = \frac{1}{2\pi K_\psi} \int_0^\pi (P_\theta g * h_\theta)(x\cos\theta + y\sin\theta)\, d\theta, \tag{9}$$

where

$$h_\theta(u) = \frac{1}{u^2} \int_0^{uT} w C_\theta(w) dw. \tag{10}$$

It can be shown that $h_\theta(u)$ is continuous at 0, and with proper choice of wavelet it can be made to decay like $1/u^2$. We see that once the convolution has been performed, the only other computation needed to reconstruct g is integration with respect to θ.

Accordingly, we will "chirp" the function $h_\theta(u)$ when viewing the scene from direction θ, and reconstruct the image domain by summing the resulting data over the entire image domain. We note that if the wavelet ψ is radially symmetric, then C_θ and hence h_θ will be independent of θ.

4 Discussion and analysis

Our method is analogous to a known method (see [5]) based on the Fourier transform. The usual formula employed by the backprojection algorithm is

$$\frac{1}{2\pi} \int_0^\pi (H' f)(x\cos\theta + y\sin\theta)\, d\theta,$$

where the operator H' denotes differentiation followed by the Hilbert transform. For arbitrary functions, H' cannot be implemented by convolution in the spatial domain, and must be achieved by multiplication by $|\rho|$ in the Fourier domain. However, let us suppose that g is band-limited in the usual sense, namely, that the support of its Fourier transform is contained in a disk of radius R. Then application of H' to g can be achieved by multiplying by $\hat{q}(\rho)$ in the Fourier domain, where $\hat{q}$ is any function that equals $|\rho|$ for $|\rho| < R$. If q is the inverse Fourier transform of $\hat{q}$, then H' can be applied to g by convolving g with q in the spatial domain. Thus

$$g(x,y) = \frac{1}{2\pi} \int_0^\pi (P_\theta g * q)(x\cos\theta + y\sin\theta))d\theta.$$

In fact, if the Fourier transform of the wavelet used to derive the signal in our method vanishes in a neighborhood of the origin, it can be shown that there exists $R > 0$ such that $\hat{h_\theta}(\rho) = |\rho|$ for $|\rho| < R$.

Let us summarize the proposed algorithm, combining the advantages of convolution backprojection and spatial filtering.

- We choose a wavelet ψ that is pseudo-symmetric and satisfies condition (7). Using ψ, we construct the chirp signal $h_\theta(t)$ for each value of θ.
- Initialize $g(x, y) = 0$ for all (x, y).
- For each available θ in the range of available angles:
  - Chirp the function $h_\theta(t)$ and record the return signal $r_\theta(t)$.
  - For each position (x, y) in the image domain, increment $g(x, y)$ by $r_\theta(x \cos\theta + y \sin\theta)$.

Note that the contribution to the image from the return signal $r_\theta(t)$ is constant along lines perpendicular to the θ direction. We see from the loop structure that it will not take long to add to g the contribution it receives from any particular value of θ, and that the contributions from different values of θ may be added to g independently. Thus, as stated above, it is quite feasible to begin the computations as soon as the first return signal is received and complete them almost immediately after the last return signal is received.

Note that the wavelet approach allows one to chose among many (infinitely many, in fact) different wavelets and use one particularly suited to the task. Empirical investigations will be needed to find the optimal chirp signal.

Error in the Wavelet-Based Chirp method will come from:

1. Loss of high-frequency data due to the decay of the Fourier transform of the signal;
2. Failure of the radar transmitter to produce the computer chirp accurately;
3. Sampling and incomplete coverage of the range of viewing angles;
4. Numerical inaccuracies.

Let us briefly discuss these issues in turn.

The loss of high-frequency information results in some loss of resolution and fine detail, but in the typical practical situation the scale of the objects to be observed is large enough that this loss of resolution is insignificant. The classical and CBP methods also lose high-frequency data due to band-limitedness of the signal, and some loss of high frequency data is inevitable in transmitting, receiving, and processing the signal, regardless of the signal used.

The problem of inaccuracies in the chirp would seem to be important, since the signal we are describing has a significant low-frequency component, and the lower frequencies tend to be lost in transmission and reflection. But the same problem occurs with the classical and CBP methods, in which the transmitted chirp does not contain low frequency information. The third problem, dealing with partial coverage of the range of angles, is also shared by the other two methods. But the classical and CBP methods work despite these problems. This is often explained as being a beneficial result of a high-frequency random perturbation that is applied to the reflectivity function by the physical system (see [9]). With regard to the problem of numerical accuracy, we will show that it is not difficult to compute the signal function h_θ to a high degree of accuracy, and the rest of the computations are a subset of those performed in the CBP method.

5 Experimental design

5.1 Computation of the signal

Computing $\int_0^{uT} wC_\theta(w)\,dw$ numerically, as suggested by equation (10), is not an effective way of computing h_θ, since computing the integral for relatively large w while keeping the error small would require sampling C_θ at a very large number of points, and accurate computation of the values of C_θ would itself be expensive. Instead, we begin with an analytic expression for $\widehat{C_\theta}(\rho)$, which depends on the choice of the wavelet ψ. We then analytically compute

$$\hat{\phi}(\rho) = \frac{1}{\rho}\frac{d}{d\rho}\hat{C}_\theta(\rho),$$

which is the Fourier transform of $\phi(u) = \int_{-\infty}^{uT} wC_\theta(w)\,dw$. We compute ϕ using a numerical Fourier transform and then use

$$h_\theta(u) = \frac{\phi(u) - \phi(0)}{u^2}. \tag{11}$$

The discrete Fourier transform (DFT) can be modeled as the trapezoidal approximation of the continuous Fourier transform of a function with compact support. Since $\hat{\phi}$ (for our choice of wavelet) is compactly supported, we combine fast (discrete) Fourier transforms with Romberg iteration to compute ϕ to a high degree of accuracy.

Direct evaluation of the right side of equation (11) is not suitable for small values of u, however, because of cancelation error in the numerator. We therefore compute a Taylor series for ϕ centered at zero. (There is no x^1 term in the series because ϕ is symmetric as long as the original wavelet satisfies condition (7), and thus its power series only has even exponents.) To compute the series coefficients, we compute the derivatives of increasing order at zero by numerically integrating the compactly supported function $\rho^n\hat{\phi}(\rho)$ for multiple values of n. Errors due to truncation and cancellation are controlled.

The signal $h_\theta(x)$ was derived from a radially symmetric wavelet whose Fourier transform is C^∞ and compactly supported and vanishes in a neighborhood of the origin. The wavelet ψ is defined by $\hat{\psi}(\rho\cos\theta, \rho\sin\theta) = \eta(|\rho|)$, where

$$\eta(\nu) = \begin{cases} \exp\left(\frac{64}{(\nu-40)^2-64}\right) & \text{if } (\nu-40)^2 < 64 \\ 0, & \text{otherwise.} \end{cases}$$

The function $h_\theta(x)$ was computed at $x_i = i/100$, where $i = -512, -511, \ldots, 512$. The vector $h_\theta(x_i)$ was padded with zeroes in order to accurately compute the convolution of the chirp signal with the image-domain data, and the DFT of the padded function was computed using an FFT algorithm. The DFT is only used to simulate the spatial domain convolution. Figure 3 displays plots of the resulting signal and its Fourier transform. Note that the duration of the chirp is less than 50 nanoseconds, and that the modal frequency of the chirp is about one Gigahertz.

5.2 Simulation of the return signal

For images defined by mathematical functions, Radon transforms were computed using Simpson's rule and Romberg iteration for 40 viewing angles equally spaced over the range of viewing angles.

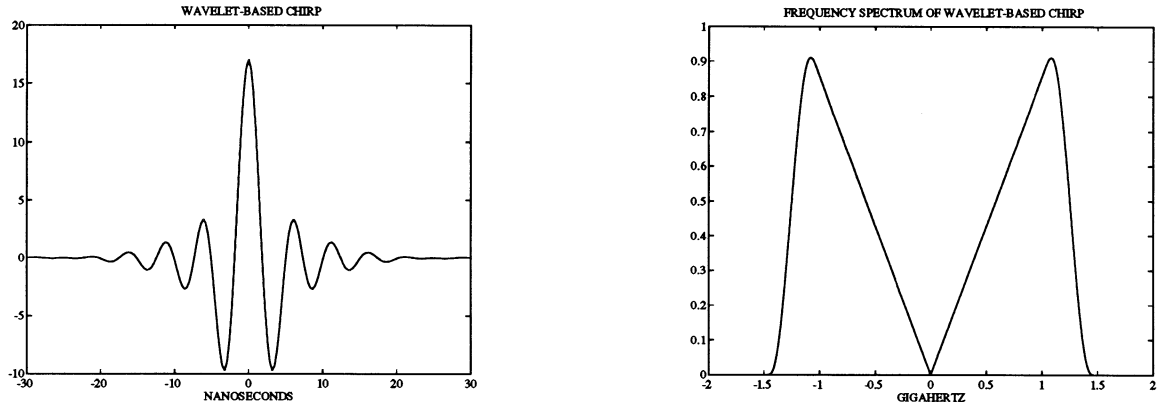

Figure 3: Left, transmitted signal. Right, its frequency spectrum.

For each viewing angle, the Radon transform was computed at the same u values for which discrete values of the signal are available, in order to convolve the signal with the Radon transform. As the lines of integration for the Radon transform fell outside the support of the image for large u, this in effect meant that the Radon transform was padded with zeroes. The procedure was the same for grayscale images, except that the Radon transforms were computed exactly, without iteration, by treating each pixel as a square and assuming that the image was constant in that square.

The convolution was effected by multiplying the DFT of the Radon transform, computed by an FFT, by the DFT of the signal, and taking the inverse DFT of the result. Normally, multiplying the DFT's of two vectors is equivalent to the circular convolution of the vectors; since here we need the convolution in the integral sense, not a circular convolution, it was necessary to pad the signal and the Radon transform with zeroes. The result of the convolution was smeared over a 500 by 500 grid.

6 Results

What follows are results of reconstructions using the Wavelet-Based Chirp method. The first function, $f_1(x, y)$, is given by

$$f_1(x,y) = \begin{cases} e^{-2(x-1.2)^2-2(y+0.5)^2} + 4e^{-(x+0.1)^2-(y-0.5)^2} - 2e^{-x^2-y^2} & \text{if } \sqrt{x^2+y^2} \leq 2.5 \\ 0 & \text{otherwise} \end{cases}$$

The second function, $f_2(x, y)$, is the characteristic function of the set S in the coordinate plane, where S is the union of the square-shaped open region $-2 < x < 0, -1 < y < 1$ and the ellipse-shaped open region

$$(x - 1/2)^2 + \frac{y^2}{(3/2)^2} < 1.$$

Figures 4 and 5 both show a surface plot of one of these functions and its respective reconstruction.

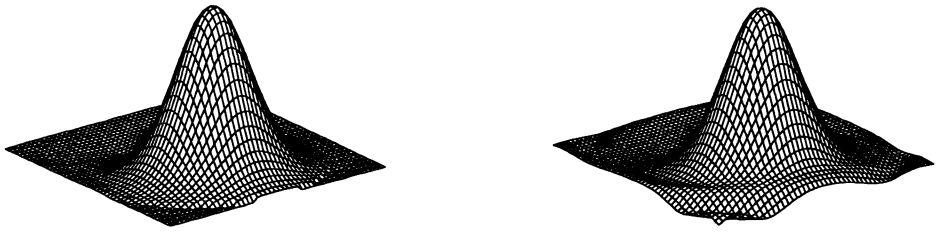

Figure 4: 3-D plots of function f_1, left, and its reconstruction, right.
The reconstruction simulates the wavelet-based chirp method.

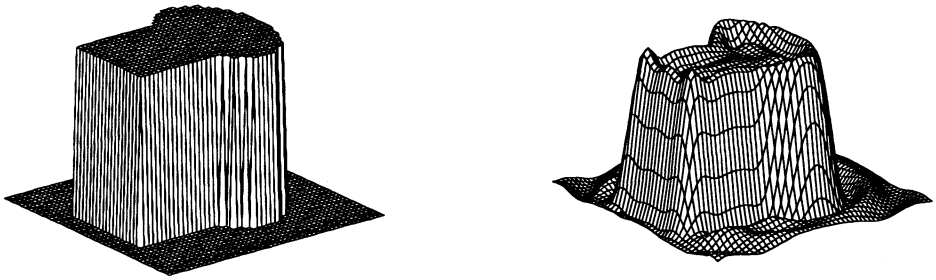

Figure 5: 3-D plots of function f_2, left, and its reconstruction, right.
The reconstruction simulates the wavelet-based chirp method.

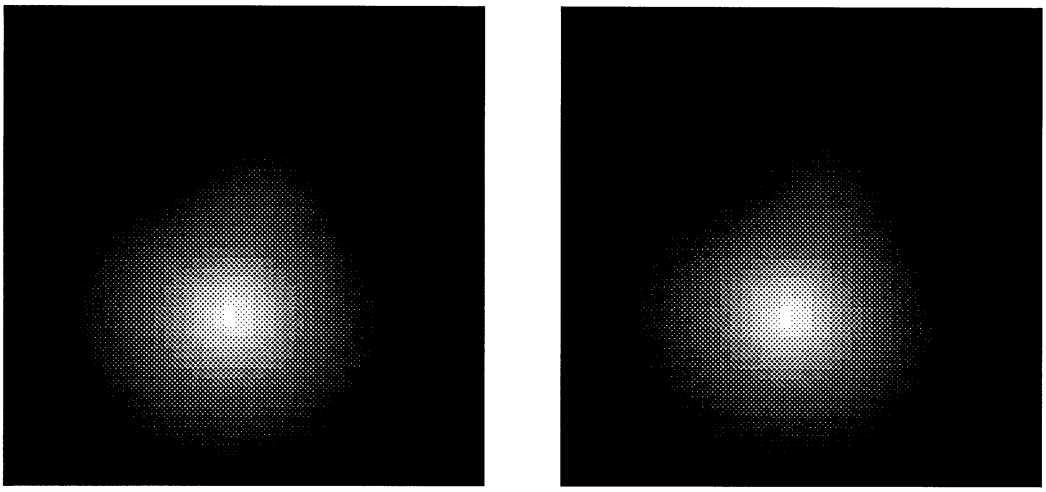

Figure 6: Grayscale images of function f_1, left, and its reconstruction, right.

In Figures 6 and 7, gray-scale versions of the same functions and reconstructions are shown. We see that low-frequency information is accurately reproduced, and that some ringing of the high-frequency information is observed.

In Figure 8, we see a grayscale image, which is used to model a complicated spatially-varying radar reflectivity function. Assuming that the chirp signal of Figure 3 is used, where the peak frequency is 1 GHz, the size of the image domain is 49 by 49 meters, and the reconstructed image, refined using a histogram equalization, is shown on the right of Figure 8.

References

[1] W.M. Boerner, C.M Ho, and B.Y. Foo, "Use of Radon's projection theory in electromagnetic inverse scattering," *IEEE Transactions on Antennas and Propagation*, vol. AP-29, no. 2, Mar. 1981, pp. 336–341.

[2] I. Daubechies, *Ten Lectures on Wavelets.* Philadelphia: Society for Industrial and Applied Mathematics, 1992.

[3] M.D. Desai, "A new method of synthetic aperture radar image reconstruction using modified convolution backprojection algorithm," Ph.D. dissertation, Univ. of Illinois, 1985.

[4] M.D. Desai, W.K. Jenkins, "Convolution backprojection image reconstruction for spotlight mode synthetic aperture radar," *IEEE Transactions on Image Processing*, vol. 1, no. 4, Oct. 1992, pp. 505–517.

[5] A. Kak, "Computerized tomography with x-ray, emission, and ultrasound sources," *Proceedings of the IEEE*, vol. 67, no. 9, Sep. 1979, pp.1245–1272.

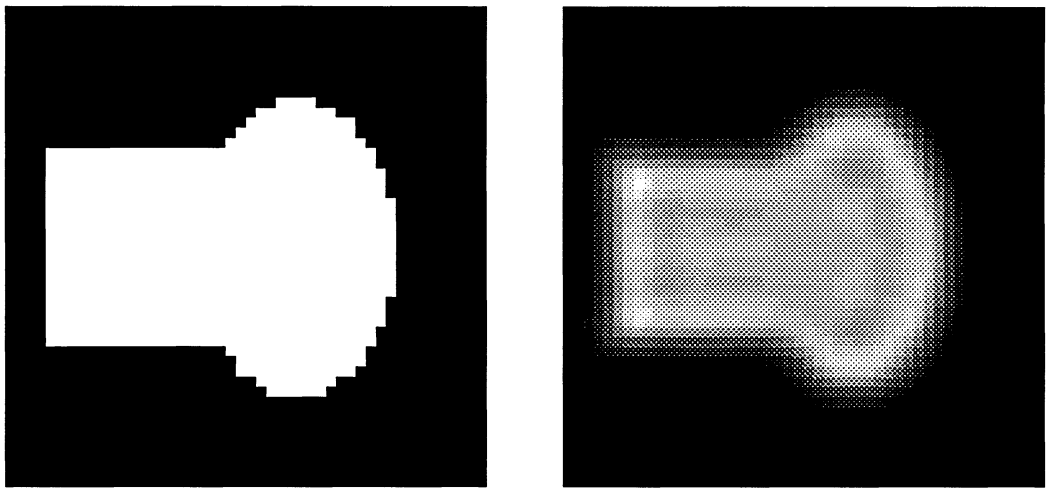

Figure 7: Grayscale images of function f_2, left, and its reconstruction, right.

[6] S. Mallat, "Multifrequency channel decompositions of images and wavelet models," *IEEE Transactions on Acoustical Signal and Speech Processing*, vol. 37, no. 12, Dec. 1989, pp. 2091–2110.

[7] R. Mersereau and A. Oppenheim, "Digital reconstruction of multidimensional signals from their projections," *Proceedings of the IEEE*, vol. 62, no. 10, Oct. 1974, pp. 1319–1338.

[8] D.C. Munson, Jr., J.D. O'Brien, W.K. Jenkins, "A tomographic formulation of spotlight-mode synthetic aperture radar," *Proceedings of the IEEE*, vol. 71, no. 8, Aug. 1983, pp. 917–925.

[9] D.C. Munson, Jr. and J.L.C. Sanz, "Image reconstruction from frequency-offset fourier data," *Proceedings of the IEEE*, vol. 72, no. 6, June 1984, pp. 661-669.

[10] S. Plimpton, G. Mastin, D. Ghiglia, "Synthetic aperture radar image processing on parallel supercomputers," Supercomputing 91 Proceedings, Albuquerque, Nov. 91, IEEE Computer Science Press: Los Alamitos, CA, pp. 446-452.

[11] J. Radon, "Uber die Bestimmung von Funktionen durch ihre Integralwärte längs gewisser Männigfaltigkeiten (On the determination of functions from their integrals along certain manifolds)," *Berichte über die Verhandlungen Sächsischen Akademie der Wissenschaften zu Leipzig*, 69:262, 1917.

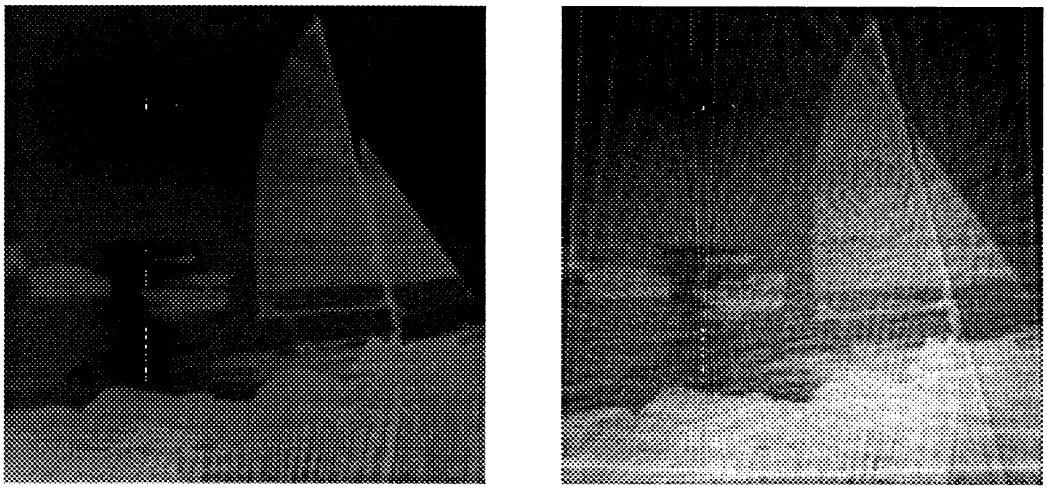

Figure 8: Left, a grayscale image of a boat. Right, its reconstruction.
The boat image is treated as the as the radar reflectivity function. There is an implicit assumption that a given spatial point has a constant reflectivity regardless of the direction of the source radar signal. The reconstruction using forty chirps at equidistant angular samples and refined using a histogram equalization is shown at right. Without the histogram equalization, the image is notably lacking in contrast. This is most probably due to drawbacks inherent in the numerical convolution used in the simulation, and thus images produced using the actual radar signals will not require histogram equalization.

1 Properties of the h_θ function

In the following, let

$$\phi(\rho) = \hat{\psi}(\rho\cos\theta, \rho\sin\theta).$$

Theorem 1.1 *If $|\phi(\rho)|^2|\rho|$ is integrable, then $h_\theta(x)$ can be defined continuously at $x = 0$.*

Proof. If $|\phi(\rho)|^2|\rho|$, the Fourier transform of C_θ, is in L^1, then C_θ is bounded and continuous. We may therefore apply the Fundamental Theorem of Calculus and apply l'Hôpital's rule twice to find that $\lim_{x\to 0} h_\theta(x) = \frac{T}{2}C_\theta(0)$.

Theorem 1.2 *Suppose ϕ is 3 times differentiable, and that $\phi(0) = \phi'(0) = 0$. Also, suppose that $\left(\frac{d}{d\rho}\right)^i (|\phi^2(\rho)\rho|)$ is absolutely integrable for $i = 0, \ldots, 3$. If, furthermore, ψ is chosen in such a way that C_θ is real, and $\psi \in L^1$, then*

$$\int_0^\infty uC_\theta(u)\,du = \frac{-2}{(2\pi)^{5/2}}C_\psi,$$

where C_ψ is the constant used in the wavelet transform inversion formula for the wavelet ψ.

It follows from the theorem that $h_\theta(x)$ decays like $\frac{\frac{-2}{(2\pi)^{5/2}}C_\psi}{x^2}$.

Remark. Since $|\phi^2(\rho)\rho| = \phi(\rho)\overline{\phi(\rho)}\,|\rho|$, and ϕ is 3 times differentiable, it is not hard to see that if ϕ is sufficiently smooth, then $\left(\frac{d}{d\rho}\right)^i (|\phi^2(\rho)\rho|)$ exists for all $i = 0, \ldots, 3$ and for all $\rho \neq 0$, so it makes sense to speak in the hypotheses of the theorem of the integrability of these derivatives.

Also note that if $\psi \in L^1$, then $\hat{\psi}$ is continuous, and therefore the wavelet admissibility condition implies that $\phi(0) = \hat{\psi}(0,0) = 0$. Also, if ψ is radially symmetric, then so is $\hat{\psi}$, and therefore ϕ is an even function. Thus ϕ' is an odd function, so $\phi'(0) = 0$. And if $\hat{\psi}$ has derivatives of orders ≤ 3, then clearly ϕ is 3 times differentiable. Thus in the hypotheses of the preceding lemma and theorem, "$\psi \in L^1$" can replace "$\phi(0) = 0$," "ψ is radially symmetric" can replace "$\phi'(0) = 0$," and "$\hat{\psi}$ has derivatives of orders ≤ 3" can replace "ϕ is 3 times differentiable".

Proof. It is not hard to show that if $f(x)$ is 3 times differentiable for all x, and $f(0) = f'(0) = f''(0) = 0$, then $|x|f(x)$ is 3 times differentiable, even at $x = 0$. It is also not hard to show that the hypotheses on ϕ imply that $|\phi(\rho)|^2$ is 3 times differentiable and $\left(\frac{d}{d\rho}\right)^i (|\phi(\rho)|^2)$ vanishes at 0 for $i = 0, 1, 2$. Thus

$$\widehat{C_\theta}(\rho) = |\phi^2(\rho)\rho|$$

is 3 times differentiable, and the hypotheses also imply that $\widehat{C_\theta}$ and its 3 derivatives are absolutely integrable. This implies that C_θ is bounded and that $|C_\theta(u)| \leq K/|u|^3$, so of

course uC_θ is bounded and $|uC_\theta(u)| \leq K/|u|^2$. Thus $C_\theta(u)$ and $uC_\theta(u)$ are absolutely integrable, and by the well-known rules for differentiation of a Fourier transform,

$$\mathcal{F}\{uC_\theta(u)\}(\rho) = i\frac{d}{d\rho}[|\phi(\rho)|^2|\rho|] = i[|\rho|\frac{d}{d\rho}((\text{Re }\phi(\rho))^2 + (\text{Im }\phi(\rho))^2) + \text{sgn}(\rho)|\phi(\rho)|^2],$$

where $\mathcal{F}$ indicates the Fourier transform. Since $uC_\theta(u)$ is an odd function, we have

$$\int_0^\infty uC_\theta(u)\,du = \frac{1}{2}\int_{-\infty}^\infty \text{sgn}(u)\,uC_\theta(u)\,du,$$

which, by the Plancherel identity, equals
PLANCHEREL LEGAL HERE?

$$\frac{1}{2}\int_{-\infty}^\infty \mathcal{F}\{\text{sgn}(u)\}(\rho)\,\overline{\mathcal{F}\{uC_\theta(u)\}(\rho)}\,d\rho = \frac{1}{2}\int_{-\infty}^\infty -i\sqrt{\frac{2}{\pi}}\frac{1}{\rho}(-i)\frac{d}{d\rho}[|\phi(\rho)|^2|\rho|]d\rho$$

$$= \frac{-1}{\sqrt{2\pi}}\int_{-\infty}^\infty \text{sgn}(\rho)\frac{d}{d\rho}((\text{Re }\phi(\rho))^2 + (\text{Im }\phi(\rho))^2) + \frac{|\phi(\rho)|^2}{|\rho|}\,d\rho. \tag{1}$$

Since $\psi \in L^1$, $\hat{\psi}$ is continuous, and therefore the admissibility requirements on ψ imply that $\phi(0) = \psi(0,0) = 0$. Thus

$$\int_0^\infty \text{sgn}(\rho)\frac{d}{d\rho}(\text{Re }\phi(\rho))^2 d\rho = \lim_{\rho\to\infty}(\text{Re }\phi(\rho))^2 - (\text{Re }\phi(0))^2 = 0.$$

We may show similarly that

$$\int_{-\infty}^0 \text{sgn}(\rho)\frac{d}{d\rho}(\text{Re }\phi(\rho))^2 d\rho = \int_0^\infty \text{sgn}(\rho)\frac{d}{d\rho}(\text{Im }\phi(\rho))^2 d\rho$$

$$= \int_{-\infty}^0 \text{sgn}(\rho)\frac{d}{d\rho}(\text{Im }\phi(\rho))^2 = 0.$$

. Thus expression (1) equals

$$\frac{-1}{\sqrt{2\pi}}\int_{-\infty}^\infty \frac{|\phi(\rho)|^2}{|\rho|}\,d\rho = \frac{-2}{(2\pi)^{5/2}}(2\pi)^2\int_{-\infty}^\infty \frac{|\phi(\rho)|^2}{|\rho|}\,d\rho = \frac{-2}{(2\pi)^{5/2}}C_\psi.$$

Lemma 1.3 *Suppose ϕ is 3 times differentiable, and that $\phi(0) = \phi'(0) = 0$. Also, suppose that $\left(\frac{d}{d\rho}\right)^i(|\phi^2(\rho)\rho|)$ is absolutely integrable for $i = 0, \ldots, 3$. Then the function*

$$\frac{vC_\theta(v)}{u^2}$$

is absolutely integrable in the infinite wedges of the u-v plane defined respectively by $0 < v < uT$ and $uT < v < 0$ for any $T > 0$.

Our remarks on the previous theorem apply here as well.

Proof. We will prove the theorem for the wedge defined by $0 < v < uT$. The proof for the other wedge is similar.

As with the previous theorem, the hypotheses imply that $vC_\theta(v)$ is absolutely integrable. Also, since $\widehat{C_\theta}$ is absolutely integrable, C_θ is bounded.

Let $P = 1/T$, and let $r^2 = u^2 + v^2$. Since $|v| \le T|u|$ in the region of integration, we find

$$r^2 = u^2 + v^2 \le u^2 + u^2T^2 = u^2(1 + T^2),$$

so

$$|u| \ge \frac{r}{\sqrt{1+T^2}}.$$

Thus

$$\left|\frac{vC_\theta(v)}{u^2}\right| \le \frac{T|C_\theta(v)|}{|u|} \le \frac{T\sqrt{1+T^2}|C_\theta(v)|}{r},$$

and the last expression is integrable near $(0,0)$, since C_θ is bounded. Thus our function is absolutely integrable in the triangle defined by $0 < u < P$, $0 < v < uT$.

USE DIAGRAM FOR THIS PROOF?

We now estimate the integral on the semi-infinite strip defined by $u > P$, $0 < v < 1$.

$$\int_{\text{strip}} \frac{|vC_\theta(v)|}{u^2}\,dv\,du = \int_0^1 |vC_\theta(v)|\,dv \int_P^\infty \frac{du}{u^2} = T\int_0^2 |vC_\theta(v)|\,dv,$$

and the last expression is finite since C_θ is bounded.

The rest of the region of integration, namely, the infinite wedge defined by $1 < v < uT$, can be thought of as the union of the sets S_n for $n \ge 1$, where S_n is the region defined by $u > nP$, $n < v < \min(n+1, uT)$. We will integrate our function on a larger set S_n', $S_n' \supset S_n$, where S_n' is the semi-infinite strip defined by $u > nP$, $n < v < n+1$. We then have

$$\int_{S_n} \left|\frac{vC_\theta(v)}{u^2}\right| dv\,du \le \int_{S_n'} \left|\frac{vC_\theta(v)}{u^2}\right| dv\,du = \int_n^{n+1} |vC_\theta(v)|\,dv \int_{nP}^\infty \frac{du}{u^2}$$

$$\le \frac{T}{n}\int_n^{n+1} \frac{K}{v^2}\,dv = \frac{T}{n}\left(\frac{1}{n} - \frac{1}{n+1}\right) < \frac{T}{n^2}.$$

Since $\sum_1^\infty \frac{T}{n^2} < \infty$, our function is absolutely integrable on the union of the S_n, so the function is absolutely integrable in the entire region of integration.

Theorem 1.4 *If the hypotheses of Lemma (1.3) are satisfied, then*

$$\int_{-\infty}^\infty h_\theta(x)\,dx = 0.$$

Proof.

$$\int_{-\infty}^{\infty} h_\theta(u)du = \left[\int_0^{\infty} du \int_0^{uT} dv - \int_{-\infty}^{0} du \int_{ut}^{0} dv\right] \frac{vC_\theta(v)}{u^2},$$

and thanks to the lemma and Fubini's theorem, we may change the order of integration in both of these integrals to find that the last expression is equal to

$$\int_0^{\infty} dv \int_{v/T}^{\infty} du \, \frac{vC_\theta(v)}{u^2} - \int_{-\infty}^{0} dv \int_{-\infty}^{v/T} du \, \frac{vC_\theta(v)}{u^2}$$

$$= \int_{-\infty}^{0} TC_\theta(v)dv + \int_0^{\infty} TC_\theta(v)dv$$

$$= T\sqrt{2\pi}\widehat{C_\theta}(0) = T\sqrt{2\pi}|\rho^2(0)|\,0 = 0.$$

It follows from this theorem that $\hat{h}_\theta(0) = 0$.

Theorem 1.5 *If the hypotheses of Theorems (1.1,1.2) and Lemma (1.3) are satisfied, then h_θ is a 1-D wavelet.*

Proof. h_θ can be thought of as the Fourier transform of $w(x) = \hat{h_\theta}(-x)$. By Theorems (1.1,1.2), $h_\theta(x)$ is continuous and decays like $1/x^2$, and is thus bounded and in L^2. Thus, by Theorem (**??**), w can be considered Hölder continuous with exponent $1/2$, and clearly so can $\hat{h_\theta}(x)$. By Theorem (1.4), whose hypotheses are the same as those of Lemma (1.3), $\int h_\theta = 0$, and therefore $\hat{h_\theta}(0) = 0$. Thus

$$|\hat{h_\theta}(x)| = |\hat{h_\theta}(x) - \hat{h_\theta}(0)| \leq C|x - 0|^{1/2} = C|x|^{1/2}$$

for some $C > 0$. This, combined with the fact that $\hat{h_\theta} \in L^2$ (since $h_\theta \in L^2$), implies that

$$\int_{-\infty}^{\infty} \frac{|h_\theta(x)|^2}{|x|} dx < \infty,$$

which is the criterion for being a wavelet.

Theorem 1.6 *Suppose the wavelet ψ used to construct h_θ satsifies $\hat{\psi}(u) = 0$ for all $\|u\| \leq R$. Then $\hat{h_\theta}(x) = C_\psi|x|$ a.e. in $\{|x| \leq RT\}$ and a.e. in θ, where C_ψ is constant used in the wavelet transform inversion formula for this wavelet.*

Proof. We claim that for $g \in L^2(\mathbb{R}^2)$ such that $\hat{g}(u) = 0$ a.e. in $\{\|u\| \geq RT\}$, $W_s g(v) = 0$ for all $s > T$ and all v, if $W_s g$ is constructed using the wavelet ψ described in the hypotheses. For

$$\widehat{W_s g}(u) = \frac{2\pi}{s}\hat{g}(u)\,\hat{\psi}\left(\frac{u}{s}\right);$$

and $\|u\| \geq RT$ implies that $\hat{g}(u) = 0$, and $\|u\| < RT \leq Rs$ implies that $\hat{\psi}(u/s) = 0$. We have shown that this implies that

$$g(x,y) = \frac{1}{2\pi C_\psi} \int_0^\pi (P_\theta g * h_\theta)(x\cos\theta + y\sin\theta)\, d\theta$$

a.e. in $\mathbb{R}^2$, and the last expression equals

$$\frac{1}{2\pi C_\psi} \int_0^\pi \int_{-\infty}^\infty \hat{g}(\rho\cos\theta, \rho\sin\theta)\, \hat{h_\theta}(\rho)\, e^{i\rho(x\cos\theta + y\sin\theta)} d\rho\, d\theta. \tag{2}$$

But computing the inverse Fourier transform of $\hat{g}$ in polar coordinates, we find that $g(x,y)$ also equals

$$\frac{1}{2\pi} \int_0^\pi \int_{-\infty}^\infty \hat{g}(\rho\cos\theta, \rho\sin\theta)\, |\rho|\, d\rho\, d\theta \tag{3}$$

a.e. in $\mathbb{R}^2$. We may therefore conclude that

$$\hat{g}(\rho\cos\theta, \rho\sin\theta)\, \hat{h_\theta}(\rho) = \hat{g}(\rho\cos\theta, \rho\sin\theta)\, C_\psi |\rho|$$

a.e. in $\{\rho \leq RT\}$, $\{\theta \in [0,\pi]\}$ for all such g. Since this holds in effect for all $\hat{g} \in L^2(\{\|u\| \leq RT\})$, the theorem is proved.